RESEARCH ARTICLE

ADVANCED ENGINEERING MATERIALS
www.aem-journal.com

$LiVO_3/LiZnVO_4$ Nanocomposite: High Performance Electrocatalyst for Ambient Nitrogen Reduction to Ammonia

*Naina Goyal, Dhamotharan Dharmasigamani, Fabio Pires, Ravi Kumar, and Sanjay Mathur**

The electrocatalytic nitrogen reduction reaction (e-NRR) has emerged as a sustainable alternative to the energy-intensive Haber–Bosch process for ammonia (NH_3) synthesis. Lithium-based electrocatalysts are particularly promising due to the high thermodynamic affinity of lithium toward nitrogen, which facilitates spontaneous N_2 adsorption to lower the activation energy required for dinitrogen dissociation. By promoting proton-coupled electron transfer and stabilizing NRR intermediates, the composite catalyst enhances reaction kinetics, enabling efficient NH_3 production. While nonaqueous lithium-containing electrolytes suppress the hydrogen evolution reaction, lithium deposition from electrolyte decomposition inhibits e-NRR. This study addresses the challenge by structurally integrating lithium into a $LiVO_3/LiZnVO_4$ nanocomposite, which channels lithium into active catalytic sites rather than parasitic plating. The oxide-oxide nanocomposite electrocatalyst delivers an ammonia yield of 53.7 $\mu g\,h^{-1}\,mg_{cat}^{-1}$ and a Faradaic efficiency (FE) of 44.8% at -0.5 V versus reversible hydrogen electrode in 0.1 M HCl electrolyte. To the best of the knowledge, this report presents a significant improvement in FE against other reported Li-mediated systems and rivalling transition metal-based catalysts.

1. Introduction

Ammonia (NH_3) is essential for the global food supply, as a key component of nitrogen-based fertilizers.[1–3] The Haber–Bosch process, responsible for industrial ammonia production, is energy-intensive with significant carbon footprints contributing to climate shift.[4,5] Electrocatalytic nitrogen reduction reaction (e-NRR) with renewable electricity offers a greener alternative to synthesize ammonia under ambient conditions. However, the Faradaic efficiency (FE) of e-NRR is impeded by two persisting challenges 1) activation of rather inert N≡N bond (941 kJ mol^{-1} dissociation energy) and 2) faster kinetics of proton reduction, feasible at lower operating potentials, outperforming e-NRR especially in water-based electrolytes. Current research efforts are directed toward identifying potential catalysts and advancing catalyst design. For example, by cooperative effects in bimetallic transition metal catalysts that offer exploiting d-orbital electron donation to populate antibonding orbitals in N_2 or employing Li-mediated catalysts that show a preferred coordination of Li^+ to weaken N≡N bonds, crucial in a viable and scalable ammonia production.[6–9]

Strategies such as the incorporation of lithium, optimization of electronic structures, and defect-engineering have improved the performance of e-NRR catalysts.[10,11] Lithium-mediated NRR in a non-aqueous electrolyte is a promising approach for suppressing parasitic reactions like the hydrogen evolution reaction (HER), due to the lack of protons. The multi-step process involves Li^+ plating → Li_xN formation → protonation, leading to NH_3 synthesis. The limited proton availability and higher nitrogen solubility in non-aqueous media enhance ammonia yield and selectivity.[12] However, this multistep process is confronted with high energy demands for Li^+ plating, dendrite formation due to anodic oxidation, and a trade-off between fast Li–N_2 reaction and slow Li_xN conversion to NH_3.[13] As an alternative, Li-mediated e-NRR using aqueous electrolytes, with water acting as an electron donor, has been proposed.[12,14] However, issues such as anodic lithium oxidation and electrode passivation persist.

Inspired by Li-mediated e-NRR, where Li-plating and Li^+ adsorption enhance catalysis, Li-containing materials have been investigated as catalysts in Li-free aqueous electrolyte. Lattice-bound Li is expected to facilitate dinitrogen reduction. For instance, Gu et al. reported $LiFeO_2$/reduced graphene oxide composite as a potential e-NRR catalyst achieving a high NH_3 yield

N. Goyal, D. Dharmasigamani, F. Pires, S. Mathur
Institute of Inorganic and Materials Chemistry
University of Cologne
50939 Cologne, Germany
E-mail: Sanjay.mathur@uni-koeln.de

D. Dharmasigamani, R. Kumar, S. Mathur
Laboratory for High Performance Ceramics
Department of Metallurgical and Materials Engineering
Research Center on Ceramic Technologies for Futuristic Mobility
Indian Institute of Technology Madras (IIT Madras)
Chennai 600036, India

The ORCID identification number(s) for the author(s) of this article can be found under https://doi.org/10.1002/adem.202501627.

DOI: 10.1002/adem.202501627

(40.5 µg h^{-1} mg_{cat}^{-1}) at −0.5 V versus reversible hydrogen electrode (RHE) and a FE of 16.4% at −0.3 V vs. RHE in 0.1 M Na_2SO_4.[15] Also, $LiMn_2O_4$ spinel nanofibers were explored for ammonia synthesis in an acidic electrolyte with 7.44% FE and 15.83 µg h^{-1} mg_{cat}^{-1} NH_3 yield at an overpotential of −0.50 V.[13] The ammonia yield of the well-known MoS_2 catalyst was found to be significantly increased upon introducing in-operando strong Li–S interaction, which effectively suppresses HER.[16] The density functional theory calculations on Li-containing bimetallic oxide revealed cooperative Li-M interactions that promote e-NRR and suppress undesired HER.[15,17]

Tyutyunnik et al. reported the alkali metal pyrovanadates for Na and K-åkermanite- type structure. However, the small ionic radii of Li^+ (0.9 Å) counteract the formation of single-phase lithium zinc vanadate åkermanite due to the relatively large coordination cavity in pyrovanadates, enabling eightfold coordination for the alkali metal cation.[18,19] Attempted synthesis of "$Li_2ZnV_2O_7$" using lithium tert-butoxide, zinc bis (trimethylsilylamide), and vanadyl isopropoxide precursors resulted in the formation of a novel $LiVO_3$/$LiZnVO_4$ nanocomposite. Due to the redox inactive electronic structure of Zn^{2+} in $LiZnVO_4$ phase, it is expected to stabilize the bimetallic catalyst. Both compounds are widely used in electrochemical energy storage.[20] In comparison to $LiVO_3$, the presence of Zn^{2+} in $LiZnVO_4$ (although both have different crystal structures) modifies the vanadium oxide framework, affecting the electronic and ionic conductivity properties.[21–27] As a result, the oxide-oxide composite ($LiVO_3$/$LiZnVO_4$) showed sevenfold increase in N_2 reduction yield compared to individual phases producing 53.7 µg h^{-1} mg_{cat}^{-1} NH_3 yield and 44.8% FE at −0.5 V versus RHE in 0.1 M HCl electrolyte under ambient experimental conditions.

2. Results and Discussion

2.1. Characterization of $LiVO_3$/$LiZnVO_4$ Nanocomposite

Figure 1a presents the powder X-ray diffractograms (XRD) of the synthesized samples $LiVO_3$, $LiZnVO_4$, and $LiVO_3$/$LiZnVO_4$ nanocomposite, with their respective joint committee on powder diffraction standards card numbers 70-1545 and 38-1332.[22,28] The synthesized composite predominantly exhibits the $LiZnVO_4$ phase along with the $LiVO_3$ phase. without any detectable crystalline impurities. Figure S1, Supporting Information, displays the XRD of the as-synthesized xerogels, while Figure S2, Supporting Information, illustrates the effect of increasing calcination temperature from 400 to 700 °C on the $LiVO_3$/$LiZnVO_4$ xerogel for 2 h. At 400 °C, crystallization of $LiZnVO_4$ is evident, and subsequent increased XRD peak intensities are observed for higher temperatures as thermal energy during coarsening drives grain growth and densification.[29] As a consequence, the crystallization of $LiVO_3$ in

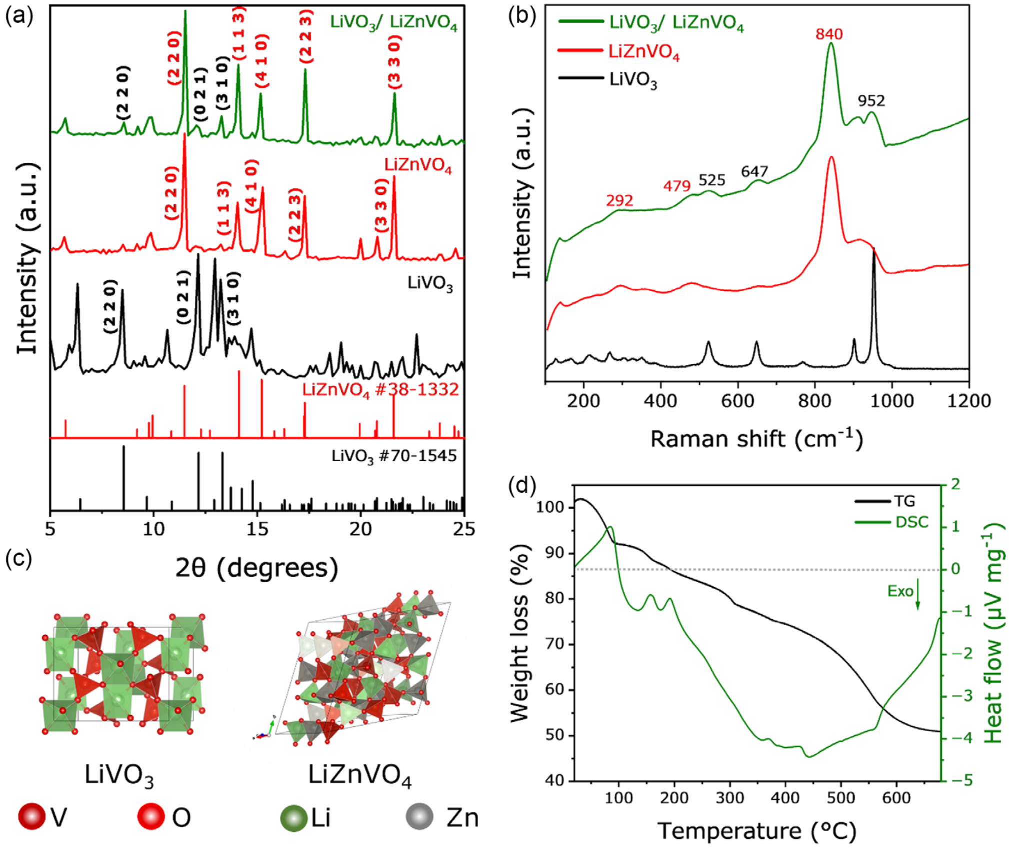

Figure 1. a) Powder XRD of the $LiVO_3$/$LiZnVO_4$ composite and individual phases, including the standard reference. b) Raman spectra of the synthesized composite and individual phases. c) Atomic cell structure of individual phases ($LiVO_3$ and $LiZnVO_4$). d) TGA-DSC measurement of as-prepared $LiVO_3$/$LiZnVO_4$ xerogel.

this composite system becomes more prominent around 500 °C. The XRD of the sample calcined at 700 °C exhibits peak broadening, which may indicate structural reconstruction prior to melting, as the powder diffused onto the crucible. The calcination beyond 700 °C was not performed, as $LiVO_3$ melted at this temperature.

For individual phase formation, the dried $LiVO_3$ xerogel was calcined at 500 °C for 2 h, resulting in a monoclinic structure (space group: C2/c).[30] Pure $LiZnVO_4$ was obtained by quenching in air after 10 min at 650 °C, as slow cooling promotes some $LiVO_3$ crystallization. The resulting structure adopts a rhombohedral crystal structure (space group: R3 (146)) with a trigonal phenacite-type arrangement (Figure 1c).[31]

The thermal behavior of $LiVO_3/LiZnVO_4$ xerogel after sol–gel processing was also analyzed using thermogravimetric analysis (TGA) and differential scanning calorimetry (DSC) under an argon atmosphere at a heating rate of 20 °C min^{-1} up to 700 °C (Figure 1d). The TG/DSC results revealed two major decomposition events occurring in the range 20–500 °C. The initial endothermic decomposition (20–90 °C) is attributed to the evaporation of chemically bonded water and alcohol molecules, while the subsequent exothermic mass loss (90–450 °C) corresponds to the decomposition of organic oxo- and hydroxy-ligands formed during the hydrolysis step. The DSC data indicate a melting event beyond 650 °C.[32] The apparent discrepancy between the melting temperatures observed in TG and XRD analyzes may stem from environmental effects during the measurements. Specifically, the TGA was conducted under an inert argon atmosphere, whereas calcination for oxide-oxide nanocomposite synthesis occurred in air, potentially allowing oxidation or other surface reactions to shift thermal behavior or phase evolution during heating.[25,33,34]

The Raman spectroscopy was used to investigate the local structure of the $LiVO_3/LiZnVO_4$ composite and compare it with the individual phases (Figure 1b). In accordance with the Raman spectra of $LiVO_3$, V–O–V vibrations are observed in the medium-frequency region (500–650 cm^{-1}), while strong V–O vibrations appear in the high-frequency region at 952, 926, and 903 cm^{-1} for both $LiVO_3$ and $LiZnVO_4$. Li–O vibrations are identified at 479 cm^{-1}. The low-frequency region (120–260 cm^{-1}) corresponds to the external modes of the VO_4^{3-} groups in $LiVO_3$. An intense peak at 840 cm^{-1} in $LiZnVO_4$ is attributed to the asymmetric and symmetric stretching vibrations of the VO_4 group, while the band at 292 cm^{-1} corresponds to Zn–O vibrations.[23,28,35] Additionally, Figure S3, Supporting Information, compares the Fourier transform infrared spectra of the as-synthesized xerogel and calcined $LiVO_3/LiZnVO_4$.

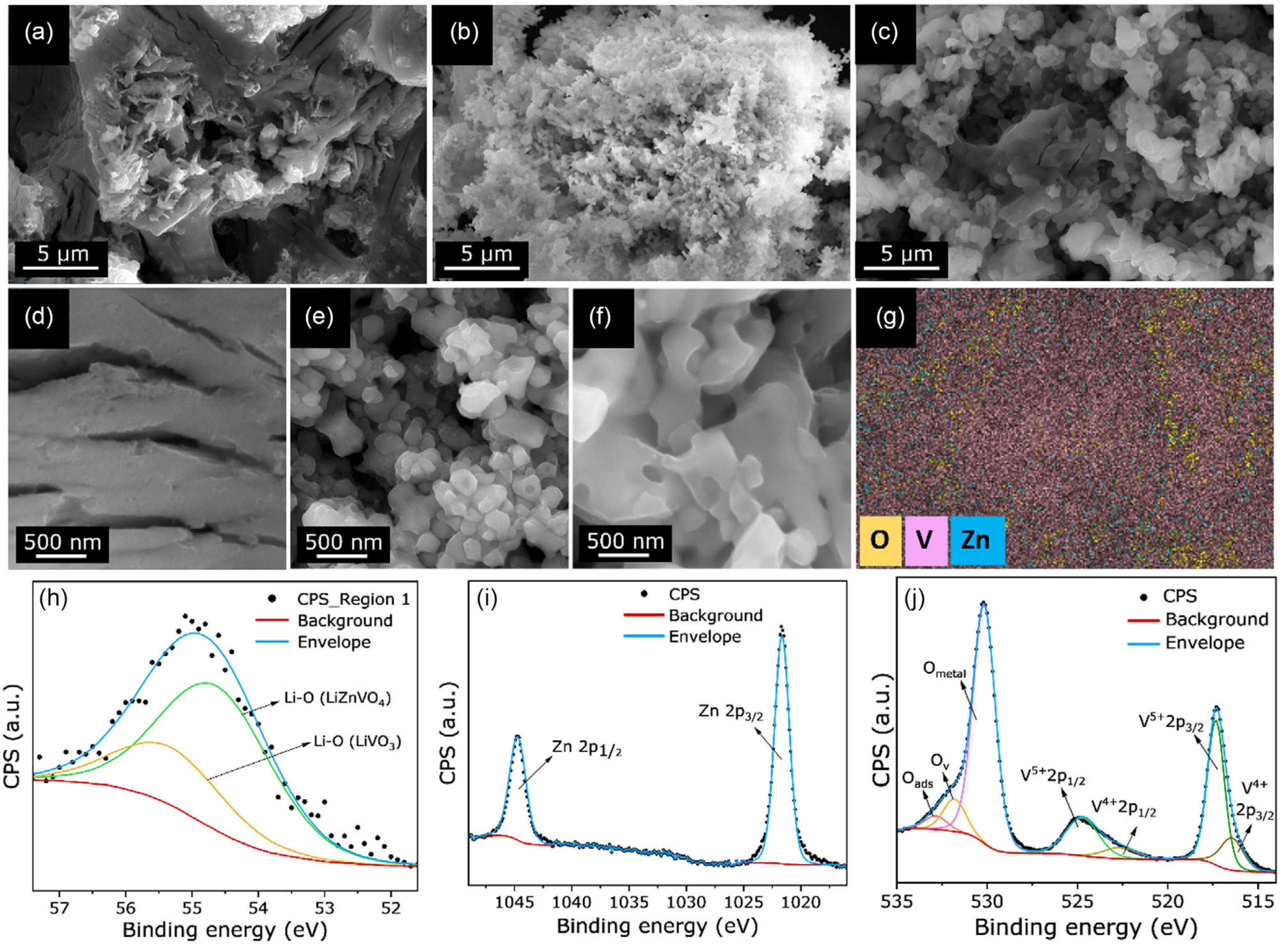

Figure 2. SEM images of synthesized individual phases: a,d) $LiVO_3$, b,e) $LiZnVO_4$, c,f) $LiVO_3/LiZnVO_4$ composite, g) EDX elemental maps corresponding to (c) SEM image, followed by XPS spectra of $LiVO_3/LiZnVO_4$ composite with high resolution: h) Li 1*s*, i) Zn 2p, and j) O 1*s*, V 2*p*.

The morphology of individual phases and the in situ synthesized composite was observed via secondary electron scanning electron microscopy (SEM) at different magnifications (**Figure** 2a–f). The individual phases $LiVO_3$ and $LiZnVO_4$ clearly present porous surface morphology with smooth plate-like structure in $LiVO_3$ (Figure 2a,d) and agglomerated fused particles of $LiZnVO_4$ (Figure 2b,e). As a result, the $LiVO_3/LiZnVO_4$ composite shows a combination of these two morphologies homogenously merged with each other (Figure 2c,f). Additionally, Figure 2d and S4, Supporting Information, confirms the presence of all expected elements like zinc, vanadium, and oxygen in Energy dispersive X-ray analysis (EDX). The selective presence of zinc additionally confirms the presence of a dual phase in the synthesized composite.

Further information on chemical composition and oxidation states was obtained from X-ray photoelectron spectroscopy (XPS) measurements. The XPS survey spectrum and deconvoluted C 1s peak from adventitious surface carbon are provided in the Supporting Information for energy calibration and confirmation of surface cleanliness (Figure S5, Supporting Information). While Li^+ is coordinated with both VO_4^{3-} and ZnO_4^{2-} tetrahedra in $LiZnVO_4$, coordination in $LiVO_3$ is octahedrally oriented with VO_4^{3-} tetrahedra. As ZnO_4^{2-} is a weaker electron-withdrawing unit compared to VO_4^{3-}, lower effective nuclear charge (Z_{eff}) values should be expected for Li—O bonds in $LiZnVO_4$ compared to $LiVO_3$. Such an effect was assigned for the deconvolution of Li 1*s* spectra (Figure 2h), with Li—O component for $LiZnVO_4$ at 54.8 eV and for $LiVO_3$ at 55.5 eV.[36] Zn 2p sharp doublet (Figure 2i), at 1021.9 eV (Zn $2p_{3/2}$) and 1044.9 (Zn $2p_{1/2}$), indicates Zn^{2+} presence from the ZnO_4^{2-} tetrahedrons of the trigonal phenacite crystal structure of $LiZnVO_4$, with signature splitting of 23 eV between the components.[37]

Moreover, O 1*s* high-resolution spectrum (Figure 2j) reveals a typical oxygen-metal main lattice peak (O_{metal}) at 530 eV, an oxygen signal related to the vicinity of oxygen-deficient species (O_v) at 531.8 eV, and oxygen-rich adsorbates (O_{ads}) at 532.9 eV.[38,39] The overlapping V 2p doublet exhibits V^{5+} $2p_{3/2}$ component at 517.3 eV and V^{5+} $2p_{1/2}$ at 524.7 eV, in agreement with 7.4 eV splitting of the 2p orbital in this oxidation state and $2p_{1/2}$ broadening.[24,40] Interestingly, the emergence of V $2p_{3/2}$ (516.5 eV) and V $2p_{1/2}$ (522.6 eV) peaks in lower binding energy suggests the presence of V^{4+} in the composite, corroborating that charge compensation takes place in the presence of defects such as oxygen vacancies (O_v) observed.[24]

2.2. Electrocatalytic NRR Activity

The electrochemical NRR efficacy of $LiVO_3/LiZnVO_4$ and individual phases was evaluated by various electrochemical measurements in a two-chambered H-cell (Figure S6, Supporting Information). Initially, the composite catalyst was examined in different pH environments, like alkaline (0.1 M KOH), neutral (0.1 M Na_2SO_4), and acidic (0.1 M HCl) through linear sweep voltammetry (LSV) performed in N_2 and control measurement in Ar-saturated electrolyte. **Figure** 3a shows a significant current

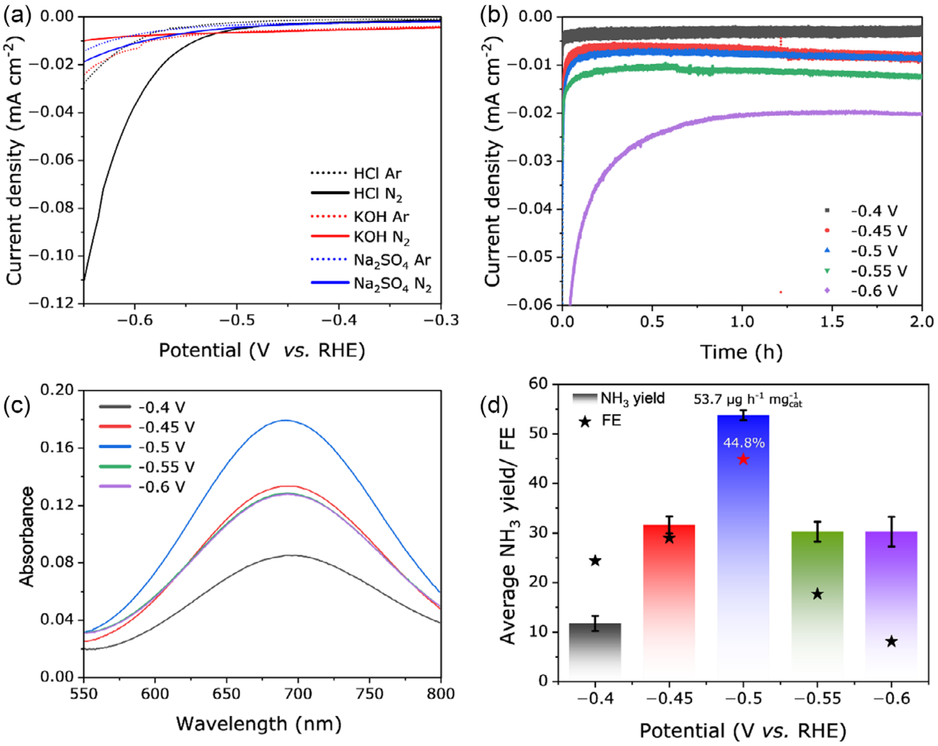

Figure 3. a) Linear sweep voltammograms of the $LiVO_3/LiZnVO_4$ catalyst in 0.1 M KOH, 0.1 M Na_2SO_4, and 0.1 M HCl electrolyte purging with Ar- and N_2- at a scan rate of 10 mV s^{-1}. b) Chronoamperometry curves for 2 h of the NRR by the $LiVO_3/LiZnVO_4$ catalyst in 0.1 M HCl electrolyte at applied potentials from −0.4 to −0.6 V. c) UV–Vis spectroscopy curves obtained after the NRR depicting ammonia formation and d) Comparison of FE and NH_3 production yield rate measured after chronoamperometry by the $LiVO_3/LiZnVO_4$ catalyst.

density enhancement in 0.1 M HCl, demonstrating potential activity of the synthesized composite in a proton-rich environment possibly due to HER suppression by Li metal in the electrocatalyst. In comparison, the same catalyst shows only a slight net current density increment in alkaline and neutral environments for nitrogen reduction, presenting deprived HER and NRR in these pH conditions. The comparison with Na_2SO_4 and KOH allows us to assess the role of proton availability in N_2 activation and ammonia formation, and to confirm that the observed activity is not solely due to acidic conditions. This clarifies 0.1 M HCl as an optimized electrolytic configuration for performing successive quantitative ammonia analysis. The LSV measurement of $LiVO_3/LiZnVO_4$ catalyst during Ar and N_2 purging shows an enhancement in the current density gap after −0.4 V versus RHE, indicating the initiation point of N_2 selected along with H_2 evolution. The quantitative analysis of produced ammonia and FE was evaluated with a combination of the charge utilized during chronoamperometry tests and calorimetric indophenol blue measurement. Figure S7, Supporting Information, shows the standard calibration curve utilized for the production of NH_3 concentration determination. The chronoamperometry was performed for 2 h at various consecutive potentials from −0.4 to −0.6 V versus RHE within −0.05 V step followed by ammonia concentration analysis via UV–Vis absorption spectroscopy (Figure 3b,c). On applied potential of −0.5 V versus RHE, catalyst $LiVO_3/LiZnVO_4$ exhibited a notable NH_3 yield rate of 53.7 μg h^{-1} mg_{cat}^{-1} and the FE reached a maximum of 44.8% FE, which is comparatively higher than other reported lithium-based catalysts for e-NRR so far (Figure 3d and **Table 1**). The ammonia yield and FE sharply decline on further negative potential increased beyond −0.5 V versus RHE possibly contributed to competitive HER evolution.

To analyze the e-NRR activity of individual phases, similar experiments were performed at −0.5 V in 0.1 M HCl separately. **Figure 4**b shows chronoamperometry of $LiVO_3$, $LiZnVO_4$, and $LiVO_3/LiZnVO_4$ catalyst compared to analyze the e-NRR activity

Table 1. e-NRR activity comparison of reported Li-based catalysts in aqueous electrolyte.

Catalyst	Electrolyte	NH_3 yield [μg h^{-1} mg_{cat}^{-1}]	Overpotential [V vs. RHE]	FE [%]	Reference
$LiMn_2O_4$	0.1 M HCl	15.83	−0.5	7.44	[13]
$LiFeO_2$/reduced graphene oxide	0.1 M Na_2SO_4	40.5	−0.5	16.4	[15]
$LiNb_3O_8$	0.1 M Na_2SO_4	7.85	−0.4	82.83	[48]
$LiFe_5O_8$/reduced graphene oxide	0.1 M HCl	36.02	−0.2	13.08	[17]
$LiVO_3/LiZnVO_4$ composite	0.1 M HCl	53.7	−0.5	44.80	This work

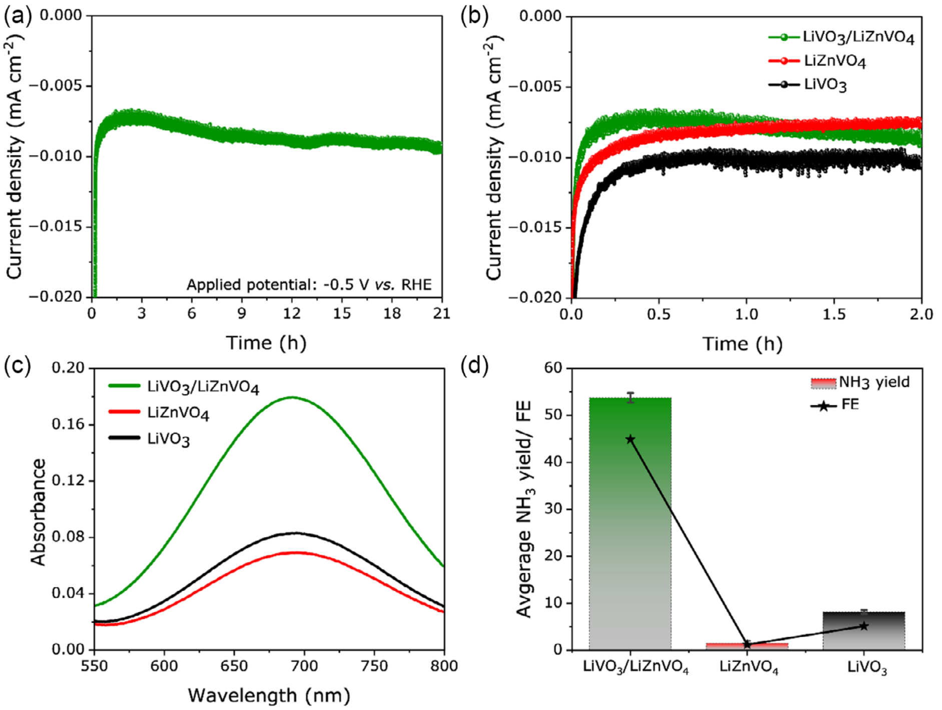

Figure 4. Chronoamperometry curves for a) 21 h of the NRR by the $LiVO_3/LiZnVO_4$ catalyst and b) $LiVO_3/LiZnVO_4$ and its constituent phases in 0.1 M HCl electrolyte at applied potentials of −0.5 V versus RHE. c) UV–Vis spectroscopy curves obtained after the NRR for all catalysts. d) Comparison of FE and NH_3 production yield rate measured after chronoamperometry by the $LiVO_3/LiZnVO_4$ catalyst and Individual phases.

represented by Figure 4c,d by the indophenol method photometric curve, and thereafter the calculated value. Both of the individual phases were observed with very inferior e-NRR activity of 5.12 μg h^{-1} mg^{-1} and 1.2 μg h^{-1} mg^{-1} with low FE of 11.5 and 2.12% which is more than seven times less than their NRR activity as a composite catalyst.[41] This value justifies the synergistic effect of both phases in $LiVO_3/LiZnVO_4$ composite catalyst to develop it as a better NH_3 producer than its constituent individual phases with maximum charge utilization for NRR rather than HER. This was further supported by high double-layer capacitance (C_{dl}) of 3.72 mF and electrochemical active surface area (ECSA) of 9.07 cm^2, suggesting a greater number of active sites in the composite catalyst compared to individual phases (Figure S8, Supporting Information).

Additionally, no catalyst leaching was confirmed by performing UV–Vis spectroscopy of the catholyte obtained after chronoamperometry (Figure S9, Supporting Information). To enlighten the superior activity of the composite catalyst, Tafel analysis were performed along with the other contributing factors, like improved active sites and selectivity of e-NRR.[42,43] Figure S10, Supporting Information, displayed the Tafel slope of $LiVO_3/LiZnVO_4$ catalyst from LSV curves in different pH conditions, which was found to be 153 mV dec^{-1} in 0.1 M HCl, which is much lower than 1628 and 299 mV dec^{-1} in 0.1 M KOH and Na_2SO_4. The lowest value of Tafel slope confirms the accelerated kinetics of $LiVO_3/LiZnVO_4$ catalyst in a proton-rich environment.

In addition to activity, stability is an important underlying factor for an electrocatalyst for its representative performance. Figure 4a shows the stability test, measured with $LiVO_3/LiZnVO_4$ catalyst by nitrogen reduction during a prolonged duration of 21 h at a constant applied potential of −0.5 V versus. RHE. The chronoamperometry shows almost no current density degradation during the stability test, validating the high durability of the catalyst. Furthermore, the reliability of the $LiVO_3/LiZnVO_4$ catalyst can be estimated by nearly identical current densities observed during both LSV and chronoamperometry measurements over 2 h, as well as in the long-term analysis.

3. Conclusions

In conclusion, this study highlights the significant role of lithium-based catalysts in ammonia production, specifically through the synthesis of an in situ $LiVO_3/LiZnVO_4$ composite material via the sol–gel method. This approach offers enhanced control over the reaction process. In contrast to individual phases, the composite catalyst demonstrated a remarkable sevenfold increase in ammonia production, achieving a yield rate of 53.7 μg h^{-1} $mg_{cat}{}^{-1}$, along with a FE of 44.8% under ambient experimental conditions with the applied potential of −0.5 V versus RHE in an aqueous acidic electrolyte (0.1 M HCl). Furthermore, the catalyst exhibited exceptional durability, maintaining current density over 21 h of stability testing. The $LiVO_3/LiZnVO_4$ composite catalyst reported in this work shows the highest ammonia yield and selectivity achieved to date among lithium-based catalysts, positioning it as a promising candidate exemplifying the role of lithium in nitrogen activation.

4. Experimental Section

The synthesis was carried out via a sol–gel approach involving cross-condensation reaction among metal alkoxides precursors: lithium tert-butoxide [$LiOC(CH_3)_3$], vanadyl isopropoxide [$VO(OCH(CH_3)_2)_3$] and the silyl amide, zinc bis (trimethylsilylamide) [$Zn(N(Si(CH_3)_3)_2)_2$], initiated through controlled hydrolysis.[33,34,44,45] The molecular alkoxide and amide were synthesized following established procedures (see supporting information) under dry nitrogen atmosphere using Schlenk line.[46,47]

Synthesis of $LiVO_3$: The precursor mixture was obtained by mixing [$LiOC(CH_3)_3$] (20 mM) and [$VO(OCH(CH_3)_2)_3$] (20 mM) in 50 mL toluene and stirring, resulting in a homogeneous solution. This multi-component solution was activated by micro-hydrolysis induced by adding 0.5 M deionized water (90 μL) in 10 mL of isopropyl alcohol that was slowly added to the precursor mixture using a dropping funnel over a period of 6 h. The mixture was stirred for another 48 h under an inert atmosphere to promote polycondensation reaction among in situ formed metal hydroxides that consequently led to a homogenous gel formation. The excess solvent was evaporated in high vacuum (10^{-3} mbar) and dried for another 12 h at 100 °C to obtain xerogel. The xerogel was calcined at 500 °C for 2 h (dwelling time) with a ramping rate of 2 °C min^{-1} to obtain black colored crystalline solid.

Synthesis of $LiZnVO_4$: An equimolar solution of each precursor in 50 mL of toluene was prepared similarly and hydrolysed by 0.5 M deionized water dissolved in 10 mL of isopropyl alcohol. Along with 48 h of stirring, solvent evaporation resulted in xerogel, which was further calcined at 650 °C for 10 min with a ramping rate of 2 °C min^{-1} and air quenched to prevent phase segregation.

Synthesis of $LiZnVO_4/LiVO_3$ Nanocomposite: A homogenous precursor solution was obtained by mixing [$LiOC(CH_3)_3$] (43.5 mM), [$Zn(N(Si(CH_3)_3)_2)_2$] (21.75 mM) and [$VO(OCH(CH_3)_2)_3$] (43.5 mM) in 50 mL toluene, with similar hydrolysis, ageing and drying conditions as used in the synthesis of individual phases. The obtained xerogel was calcined at 500 °C for 2 h with a ramping rate of 2 °C min^{-1}, resulting in $LiVO_3/LiZnVO_4$ composite, respectively.

Electrochemical Measurements: General Information: All electrochemical measurements were conducted using a PalmSens 4 potentiostat controlled via PSTrace software in a gas-tight H-cell equipped with a three-electrode configuration. An H-cell is used in NRR to physically separate the working and counter electrodes, preventing product crossover and contamination during ammonia detection. The working electrode was prepared by depositing the catalyst onto a pre-cleaned glassy carbon electrode (GCE, 3 mm diameter). An Ag/AgCl (3 M KCl) electrode served as the reference electrode in the catholyte, while a platinum spring acted as the counter electrode in the anolyte. Each compartment was filled with 50 mL of electrolyte. All potentials were referenced to the RHE using the standard conversion formula: (RHE) = E (Ag/AgCl) + 0.197 V + 0.059 pH.

Electrochemical Measurements: Working Electrode Preparation: A homogenous catalyst ink was prepared by dispersing 4 mg of finely ground catalyst powder in 190 μL of ethanol and 10 μL of Nafion D-521 (5% w/w in water and 1-propanol), followed by sonication. A total of 5 μL of the resulting slurry was drop-cast onto the GCE in two sequential steps, allowing each layer to dry at room temperature before proceeding to the next step.

Electrochemical Measurements: Electrolyte Preparation and Gas Purification Setup: Prior to each experiment, the cathodic electrolyte was degassed by purging with argon (Ar) for 30 min to remove dissolved oxygen, followed by nitrogen (N_2) saturation for an additional 30 min. To prevent ammonia overestimation, the Ar and N_2 gas streams were passed through a custom-built purification system comprising 1 M H_2SO_4 to capture $NH_4{}^+$ impurities and 0.1 M $KMnO_4$ in an alkaline solution to trap NO_x species.

Electrochemical Measurements: Ammonia Quantification: Ammonia quantification was performed via UV–Vis spectrophotometry using the indophenol blue method with a commercial ammonia detection kit. In a typical procedure, 5 mL of the electrolyte sample was mixed with 0.6 mL of Reagent 1 (sodium hydroxide-containing solution), followed by the addition of Reagent 2 (containing thymol). The mixture was allowed to stand for 5 min to ensure complete dissolution. Subsequently, Reagent 3 (containing 2-propanol) was added, and the solution was stirred and left to stand for an additional 5 min. The resulting solution was analyzed by UV–Vis absorption spectroscopy over the wavelength range of 550–850 nm. The absorbance peak intensity at ≈693 nm was used to quantify ammonia concentration based on the standard calibration curve.

For calibration curve construction, standard solutions of NH_4Cl at known concentrations (0, 0.5, 1.0, 1.5, and 2.0 μg mL^{-1}) were prepared and analyzed using the same indophenol blue protocol. The resulting calibration curve was used for quantifying ammonia yield and calculating FE.

The ammonia yield rate was calculated using the formula

$$\mathrm{NH_3\ yield} = \frac{C_{\mathrm{NH_3}} \cdot V}{m_{\mathrm{cat}} \cdot t} \tag{1}$$

where $C_{\mathrm{NH_3}}$ denotes the ammonia concentration determined from photometric test, V is the total volume of cathodic electrolyte, m_{cat} is the loaded catalyst mass and t represent the duration of electrocatalysis or chronoamperometry performed.

The FE was determined as the ratio of the charge consumed for ammonia formation to the total charge passed during electrolysis, calculated using following equation

$$\mathrm{FE} = \frac{3F \cdot C_{\mathrm{NH_3}} \cdot V}{17 \cdot Q} \tag{2}$$

where F is the Faraday constant (96 500 C mol^{-1}) and Q is the total charge passed through the system obtained by integrating the area under the chronoamperometric curve.

Supporting Information

Supporting Information is available from the Wiley Online Library or from the author.

Acknowledgements

The authors gratefully thank Deutsche Forschungsgemeinschaft (DFG) for the financial support, University of Cologne for the infrastructural support, and Center for Fuel Cell and Technology (CFCT), ARCI, for providing access to the X-ray photoelectron spectroscopy characterization facility under the MNRE Project No: 350/2/2018-NT. D.D. gratefully acknowledges the support received under the OGE Travel Grant program of the Indian Institute of Technology Madras. F.P. acknowledges the São Paulo Research Foundation (FAPESP grant 2024/05567-3). The authors also acknowledge Marios Symeonidis for thermogravimetric-differential scanning calorimetry measurements.

Open Access funding enabled and organized by Projekt DEAL.

Conflict of Interest

The authors declare no conflict of interest.

Data Availability Statement

The data that support the findings of this study are available from the corresponding author upon reasonable request.

Keywords

acid electrolyte, electrochemical nitrogen reduction, Li-based catalyst, $LiVO_3$, $LiZnVO_4$, sol–gel reaction

Received: June 17, 2025
Revised: September 2, 2025

[1] H. S. Ahmed, Z. Yahya, W. Ali Khan, A. Faraz, *Clean Energy* **2024**, *8*, 60.
[2] Z. Fang, Z. Hong, X. Ji, *AIP Conf. Proc.* **2024**, *3144*, 020005.
[3] J. Sun, D. Alam, R. Daiyan, H. Masood, T. Zhang, R. Zhou, P. J. Cullen, E. C. Lovell, A. (Rouhollah) Jalili, R. Amal, *Energy Environ. Sci.* **2021**, *14*, 865.
[4] J. Humphreys, R. Lan, S. Tao, *Adv. Energy Sustainability Res.* **2021**, *2*, 2000043.
[5] N. Erfani, L. Baharudin, M. Watson, *Chem. Eng. Process.: Process Intensif.* **2024**, *204*, 109962.
[6] D. Chanda, R. Xing, T. Xu, Q. Liu, Y. Luo, S. Liu, R. A. Tufa, T. H. Dolla, T. Montini, X. Sun, *Chem. Commun.* **2021**, *57*, 7335.
[7] X. Wen, J. Guan, *Nanoscale* **2020**, *12*, 8065.
[8] X. Zhao, G. Hu, G.-F. Chen, H. Zhang, S. Zhang, H. Wang, *Adv. Mater.* **2021**, *33*, 2007650.
[9] J. Choi, B. H. R. Suryanto, D. Wang, H.-L. Du, R. Y. Hodgetts, F. M. Ferrero Vallana, D. R. MacFarlane, A. N. Simonov, *Nat. Commun.* **2020**, *11*, 5546.
[10] M. Ismael, M. Wark, *Appl. Mater. Today* **2024**, *39*, 102253.
[11] G.-F. Chen, S. Ren, L. Zhang, H. Cheng, Y. Luo, K. Zhu, L.-X. Ding, H. Wang, *Small Methods* **2019**, *3*, 1800337.
[12] M. I. Ahmed, A. Assafiri, D. B. Hibbert, C. Zhao, *Small* **2023**, *19*, 2305616.
[13] C. Li, J. Yu, L. Yang, J. Zhao, W. Kong, T. Wang, A. M. Asiri, Q. Li, X. Sun, *Inorg. Chem.* **2019**, *58*, 9597.
[14] J. M. McEnaney, A. R. Singh, J. A. Schwalbe, J. Kibsgaard, J. C. Lin, M. Cargnello, T. F. Jaramillo, J. K. Nørskov, *Energy Environ. Sci.* **2017**, *10*, 1621.
[15] W. Gu, Y. Guo, Q. Li, Y. Tian, K. Chu, *ACS Appl. Mater. Interfaces* **2020**, *12*, 37258.
[16] Y. Liu, M. Han, Q. Xiong, S. Zhang, C. Zhao, W. Gong, G. Wang, H. Zhang, H. Zhao, *Adv. Energy Mater.* **2019**, *9*, 1803935.
[17] Y. Ji, L. Li, W. Cheng, Y. Xiao, C. Li, X. Liu, *Inorg. Chem. Front.* **2021**, *8*, 3156.
[18] A. P. Tyutyunnik, V. G. Zubkov, L. L. Surat, B. V. Slobodin, G. Svensson, *Powder Diffr.* **2005**, *20*, 189.
[19] B. V. Slobodin, L. L. Surat, *Russ. J. Inorg. Chem.* **2006**, *51*, 1345.
[20] R. Cui, J. Lin, X. Cao, P. Hao, X. Xie, S. Zhou, Y. Wang, S. Liang, A. Pan, *Inorg. Chem. Front.* **2020**, *7*, 340.
[21] M. Büyükyazi, S. Mathur, *Nano Energy* **2015**, *13*, 28.
[22] D. Yang, D. Zhang, H. Wu, T. Xiao, S. Ni, *Ionics* **2022**, *28*, 3671.
[23] N. V. Kosova, D. O. Rezepova, A. B. Slobodyuk, *Electrochim. Acta* **2015**, *167*, 75.
[24] Z. Huang, L. Cao, L. Chen, Y. Kuang, H. Zhou, C. Fu, Z. Chen, *J. Phys. Chem. C* **2016**, *120*, 3242.
[25] Z.-W. Chiu, Y.-J. Hsiao, T.-H. Fang, L.-W. Ji, *J. Sol–Gel Sci. Technol.* **2014**, *69*, 299.
[26] M. Ram, *J. Alloys Compd.* **2011**, *509*, 5688.
[27] T.-Y. An, C. Xia, M. Je, H. Lee, S. Ji, M.-C. Kim, S. Surendran, M.-K. Han, J. Lim, D.-K. Lee, J. Y. Kim, T.-H. Kim, H. Choi, J. K. Kim, U. Sim, *SusMat* **2024**, *4*, e226.
[28] B. K. Grandhe, S. Ramaprabhu, S. Buddhudu, K. Sivaiah, V. R. Bandi, K. Jang, *Opt. Commun.* **2012**, *285*, 1194.
[29] D. Gouvêa, *J. Eur. Ceram. Soc.* **2024**, *44*, 116677.
[30] R. D. Shannon, C. Calvo, *Can. J. Chem.* **1973**, *51*, 265.
[31] W.-B. Li, H.-H. Xi, D. Zhou, *Ceram. Int.* **2015**, *41*, 9063.
[32] A. E. Danks, S. R. Hall, Z. Schnepp, *Mater. Horiz.* **2016**, *3*, 91.
[33] S. Mathur, M. Veith, M. Haas, H. Shen, N. Lecerf, V. Huch, S. Hüfner, R. Haberkorn, H. P. Beck, M. Jilavi, *J. Am. Ceram. Soc.* **2001**, *84*, 1921.

[34] M. Veith, S. Mathur, A. Kareiva, M. Jilavi, M. Zimmer, V. Huch, *J. Mater. Chem.* **1999**, *9*, 3069.
[35] A. Grzechnik, P. F. McMillan, *J. Phys. Chem. Solids* **1995**, *56*, 159.
[36] W. Yu, Z. Yu, Y. Cui, Z. Bao, *ACS Energy Lett.* **2022**, *7*, 3270.
[37] F. Xie, M. Yang, Z.-Y. Song, W.-C. Duan, X.-J. Huang, S.-H. Chen, P.-H. Li, X.-Y. Xiao, W.-Q. Liu, P.-H. Xie, *Electrochim. Acta* **2022**, *426*, 140757.
[38] T. J. Frankcombe, Y. Liu, *Chem. Mater.* **2023**, *35*, 5468.
[39] F. A. Pires, G. T. dos Santos, J. Bettini, C. A. R. Costa, R. V. Gonçalves, R. H. R. Castro, F. L. Souza, *Sustainable Energy Fuels* **2023**, *7*, 5005.
[40] M. C. Biesinger, L. W. M. Lau, A. R. Gerson, R. St. C. Smart, *Appl. Surf. Sci.* **2010**, *257*, 887.
[41] E. Antolini, *Appl. Catal., B* **2010**, *100*, 413.
[42] D. Gupta, A. Kafle, T. C. Nagaiah, *Faraday Discuss.* **2023**, *243*, 339.
[43] B. Witulski, N. Goyal, D. Patrun, F. Pires, Z. Aytuna, H. Alaei, O. Schiemann, S. Mathur, *Adv. Eng. Mater.* **2025**, *27*, 2500764.
[44] M. Veith, S. Mathur, N. Lecerf, V. Huch, T. Decker, H. P. Beck, W. Eiser, R. Haberkorn, *J. Sol–Gel Sci. Technol.* **2000**, *17*, 145.
[45] Z. Aytuna, A. Bhardwaj, M. Wilhelm, D. Patrun, T. Fischer, R. Sharma, K. Papakollu, R. Kumar, S. Mathur, *J. Eur. Ceram. Soc.* **2024**, *44*, 7760.
[46] R. Yang, G. Xu, C. Lv, B. Dong, L. Zhou, Q. Wang, *ACS Sustainable Chem. Eng.* **2020**, *8*, 18347.
[47] C. N. Caughlan, H. M. Smith, K. Watenpaugh, *Inorg. Chem.* **1966**, *5*, 2131.
[48] Q. Wang, S. Fan, L. Liu, X. Wen, Y. Wu, R. Yao, Q. Zhao, J. Li, G. Liu, *Dalton Trans.* **2022**, *51*, 1131.